

Identification of fluorescent aerosol observed by a spectroscopic lidar over northwest China

YONGKAI WANG,¹ ZHONGWEI HUANG,^{1,2,*} TIAN ZHOU,¹
JIANRONG BI,^{1,2} AND JINSEN SHI^{1,2}

¹Key Laboratory for Semi-Arid Climate Change of the Ministry of Education, College of Atmospheric Sciences, Lanzhou University, Lanzhou 730000, China

²Collaborative Innovation Center for West Ecological Safety (CIWES), Lanzhou University, Lanzhou 730000, China

*huangzhongwei@lzu.edu.cn

Abstract: Bioaerosols play a significant role in climate change and variation of ecological environment. To investigate characterization of atmospheric bioaerosols, we conducted lidar measurement for observing bioaerosols close to dust sources over northwest China in April, 2014. The developed lidar system can not only allowed us to measure the 32-channel fluorescent spectrum between 343 nm to 526 nm with a spectral resolution of 5.8 nm but also simultaneously detect polarisation measurements at 355 nm and 532 nm, as well as Raman scattering signals at 387 nm and 407 nm. According to the findings, the lidar system was able to pick up the robust fluorescence signal emitted by dust aerosols. Especially the polluted dust, the fluorescence efficiency could reach 0.17. In addition, the efficiency of single-band fluorescence typically rises as the wavelength goes up and the ratio of fluorescence efficiency of polluted dust, dust, air pollutant and background aerosols is about 4:3:8:2. Moreover, our results demonstrate that simultaneous measurements of depolarization at 532 nm and fluorescence could better distinguish fluorescent aerosols than those at 355 nm. This study enhances the ability of laser remote sensing for real-time detecting bioaerosol in the atmosphere.

© 2023 Optica Publishing Group under the terms of the [Optica Open Access Publishing Agreement](#)

1. Introduction

Aerosols that contain microorganisms or are derived from biological substances and have a diameter of fewer than 100 microns are referred to as biological aerosols. Examples of biological aerosols include PM_{2.5}, PM₁₀, and other atmospheric particles that are suspended in a large number of bacteria, viruses, fungi, sensitized pollen, and parasitic ovum [1]. Bioaerosols have the potential to affect the microphysical characteristics of clouds as well as precipitation. It is also capable of taking part in chemical and physical processes in the atmosphere, as well as having an impact on atmospheric composition and radiative forcing [2]. Després et al. [3] found that bioaerosols can more efficiently and easily act as cloud condensation (CCN) or ice nuclei (IN) than most other types of aerosol particles. Ginoux et al. [4] estimated that about 2000 tons of dust are injected into the atmosphere every year. Every year, massive sandstorms release bioaerosols into the air, drastically decreasing air quality and leading to serious pollutant events that have devastating effects on human health, especially in the form of respiratory and cardiovascular diseases [5].

Extensive research confirms that indeed dust can act as a transport medium for bioaerosols over long distances [6,7]. According to data collected in Japan, bacterial levels in the air tend to rise dramatically during dust events [8]. Conditions for the emission and dispersion of bioaerosol are provided by dust, which acts as a transport carrier [9]. In their study, Prospero et al. [10] found that long-distance transport of living microorganisms may have significant contributions from arid regions. Studies by Maki et al. [11] found that bacilli are commonly found on Asian dust that has been transported outside of the region.

Currently, development of ultraviolet light-induced fluorescence (UV-LIF) instruments, such as the wideband integrated bioaerosol sensor (WIBS), the ultraviolet aerodynamic particle sizer spectrometer (UV-APS) have allowed real-time collection of aerosol information [12,13]. The principle of detection relies on the ability of bioaerosols to efficiently produce wideband fluorescence emissions when exposed to UV radiation [14]. The resulting fluorescence spectroscopy can be used to extensively classify organic compounds, whereas the fluorescence of non-organic compounds in atmospheric aerosols is typically weak [15]. Previous work has showed that differences in the autofluorescence intensity of different bioaerosols can distinguish and count bioaerosols in real time [16,17]. A strong fluorescent signal in the water-vapor Raman channel from forest-fire smoke has been reported by Immler et al. [18]. The two-wavelength excitation method has been shown to be useful for distinguishing between bacterial spores, vegetative bacterial cells, and proteins [19]. Additionally, measurements by a developed mobile laser-induced fluorescence spectrum lidar show that for the 355 nm stimulating wavelength, the fluorescence spectra of various pollen grains have maxima in the 400-600 nm range and an intensity peak at around 460 nm [20]. There have been scant spectroscopic lidar system-based studies of bioaerosols in dust in northwest China, and there is still a dearth of observation data from great heights. In April of 2014, researchers in northwest China used a new spectroscopic lidar system to observe dust-bioaerosols in the atmosphere and the vertical structure of fluorescent aerosols within the boundary layer. The system is designed for simultaneous detection of elastic and Raman backscattering, allowing the so-called $2\beta + 2\alpha + 2\delta$ data configuration, including two particle backscattering coefficients (β_{355} , β_{532}), two extinction coefficients (EXT_{355} , EXT_{532}) and two volume depolarization ratios (VDR_{355} , VDR_{532}). The paper is structured as follows: Section 2 provides a brief description of the lidar system and the data processing method, while Section 3-4 provides the results and discussion. Finally, Section 5 summarizes the conclusions.

2. Lidar system and methods

The field experiment was conducted on farmland in Linze site, Gansu Province in northwest China (39.05°N, 100.12°E); this area is situated in the middle of the Hexi Corridor (1579 m above sea level). The Hexi Corridor is a long, thin area formed by mountains on both its northern and southern sides, giving it a roughly northwest-southeast orientation. Southwest of the Badain Jaran desert, with the Taklimakan desert to the west, is where you'll find this particular spot. The ground-based lidar system of Lanzhou University was used for this campaign from 10 to 28 April 2014, which can collect the backscattering signals of 532 nm, 355 nm and 32 fluorescence channels simultaneously. The lidar system employs an Nd: YAG laser. Lasers are collimated and amplified by beam expanders. The backscattering signals are picked up by a telescope with a 400 mm aperture. Polarizing beamsplitters separate the 532 nm and 355 nm signals into their parallel and vertical components, which are then picked up by photomultiplier tubes (PMT). Using an excitation wavelength of 355 nm, a 32-channel spectrometer with spectral resolutions of 5.8 nm can detect the fluorescent spectrum from atmospheric aerosols. The spectrometer works by first transforming the signal into parallel light, then splitting it with a diffraction grating, then converting it into an electrical signal with a PMT array consisting of 32 individual photomultipliers, and finally saving the data to a computer by counting individual photons. The grating equation is:

$$d(\sin \alpha + \sin \beta) = m\lambda \quad (1)$$

where, d is the grating constant; α and β are incidence angles and diffraction angles, respectively. m is the diffraction order; λ is the diffraction wavelength.

The spectrum received by the spectrometer is continuous between 358 and 526 nanometers. The effective fluorescence spectrum was determined to be the range from 420 nm to 520 nm after taking into account the impact of atmospheric main gases like O_2 , N_2 and H_2O Raman and the dependability of spectral edge. The spatial and temporal resolution of the meter signal

are 2 min and 3.75 m, and the fluorescence signal are 3 min and 15 m, respectively. The developed Mie-Raman fluorescence spectrum UV polarization lidar that was used in this paper is illustrated with a schematic diagram in Fig. 1. The unprocessed signals were first pre-processed by subtracting the background, correcting the range, correcting the overlap, and calibrating the polarization [21–23]. Calibration of the spectrometer data is required due to the fact that the sensitivity of the response of each channel detection unit to the signal varies. The fluorescence measurements were performed at night only because of solar background radiation. It is required to calibrate the spectrometer data because each channel detection unit responds to signals with a varied degree of sensitivity [24]. The general formula is as follows [25]:

$$P_s(r) = C \frac{P_0}{r^2} O(r) \beta(r) \exp\left(-2 \int_0^r \alpha(r') dr'\right) + P_b \quad (2)$$

where P_0 and $P_s(r)$ are respectively transmitted power and received echo signal intensity; r is the distance between lidar and particulate matter; C is the lidar system constant; $O(r)$ is the geometrical overlap factor; β and α are the backscattering coefficient and extinction coefficient (EXT), respectively. P_b is the background signal, including the signal from the external environment and the noise inside the system.

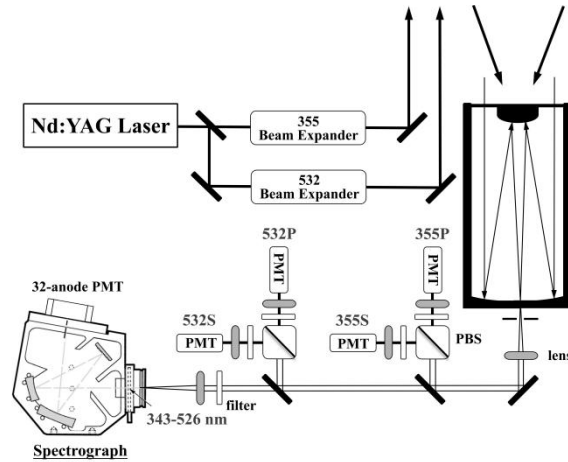


Fig. 1. Schematic diagram of the spectroscopic lidar system developed in this study.

The principle of Raman scattering between laser and matter is at the heart of Raman lidar technology [26]. If 355 nm is used as the excitation wavelength, N_2 and H_2O in the atmosphere can generate Raman frequency shift due to energy exchange, which is 387 nm and 407 nm respectively. Raman signals of N_2 can be expressed as:

$$P_{N_2}(r) = CP_0 O(r) \beta_{N_2} \exp\left\{-\int_0^r [\alpha_0(r') + \alpha_{N_2}(r')] dr'\right\} \quad (3)$$

Since there was no Raman signal at 607 nm, we determined the extinction coefficient and backscattering coefficient at 532 nm by use of the Fernald method [27,28].

The fluorescence backscattering coefficient also can be calculated from the ratio of fluorescence and N_2 Raman backscattering, as described in Veselovskii et al. [29]. The fluorescence signal in the different wavelength can be expressed as,

$$P_F(\lambda, r) = CP_0 O(r) \beta_F \exp\left\{-\int_0^r [\alpha_0(\lambda, r') + \alpha_F(\lambda, r')] dr'\right\} \quad (4)$$

The total depolarization ratio of air molecules and particles is known as the volume depolarization ratio (VDR), and its value can be utilized to differentiate between spherical and non-spherical particles, especially in dust detection [30–33]. The VDR can be calculated by multiplying the calibration factor with the ratio of vertical channel to parallel channel and the ratio of VDR_{532}/VDR_{355} is defined as a parameter to distinguish dust and pollutant [34]:

$$VDR = \frac{P_{\perp}}{P_{\parallel}} \quad (5)$$

The color ratio (CR) is related to the size of aerosols, in which large color ratios corresponds to coarse particle [35]:

$$CR = \frac{P_{532}}{P_{355}} \quad (6)$$

We calculated the fluorescence efficiency (η) according to the method of Sugimoto et al. [36], whose experiment proved that the fluorescence efficiency could effectively reflect the fluorescence of aerosols.

$$\eta = f \frac{SSA}{1 - SSA} \cdot \frac{\beta_F}{\beta} \quad (7)$$

Here, β_F is the backward fluorescence coefficient, β is the backscattering coefficient and η is the fluorescence efficiency. The factor f represents the difference between the Mie scattering phase function and that for fluorescence. SSA is the aerosol single-scattering albedo. Since there is no measured data, in this study, it is assumed that the SSA of dust and background aerosol is 0.9, that of polluted dust is 0.95, and that of air pollutant is 0.99 [36,37].

Figure 2 displays the results of the observations of $PM_{2.5}$ and the absorption coefficient in rural Linze. $PM_{2.5}$ was collected by TEOM RP1400 and the absorption coefficient was calculated from the black carbon concentration obtained by the AE31. During non-pollution times, both $PM_{2.5}$ and absorption coefficient were low, but during polluted times, they rose dramatically. Recent decades have seen research into using lidar data for the purpose of identifying aerosol types [38–40]. Müller et al. [41] have reported that the wavelength dependence of the lidar ratio can be used to distinguish urban aerosols from smoke aerosols. Depolarization color ratio was found to be useful in characterizing smoke from biomass burning and urban pollution by Foy et al. [42]. The work of Burton et al. [43] builds upon that of previous researchers by using the HSRL's measurements of aerosol intensive parameters to develop a comprehensive and unified set of rules for characterizing the external mixing of several key aerosol intensive parameters. These include the lidar ratio, the backscatter color ratio, and the depolarization ratio. According to studies conducted by Filonchik et al. [44], the peak seasons for pollution in northwest China are the winter and spring months. This is because dust activity increases in the spring, while household heating systems release more pollutants in the winter. Because of this variability in composition, the optical and radiative properties of atmospheric aerosols are altered by their presence. Based on lidar data and in-situ observations, four types of aerosols were chosen for further study. Shadows in blue represent background aerosol, yellow dust, green polluted dust, and gray air pollutants.

2.1. Characteristics of background aerosol over the observation site

Aerosol over the observation site is affected not just by dust, but also by human activities, particularly those related to local agricultural and animal husbandry [45], as shown by long-term observations conducted at the University of Lanzhou. Background aerosol characteristics, including EXT, VDR, CR and VDR_{532}/VDR_{355} at two wavelengths, were observed on 20-21 April 2014, and are displayed vertically in Fig. 3 (b,c,e,f). The EXT at both wavelengths were close, varying in the $0.1\text{-}0.3\text{ km}^{-1}$ range, which indicates that the aerosol concentration was

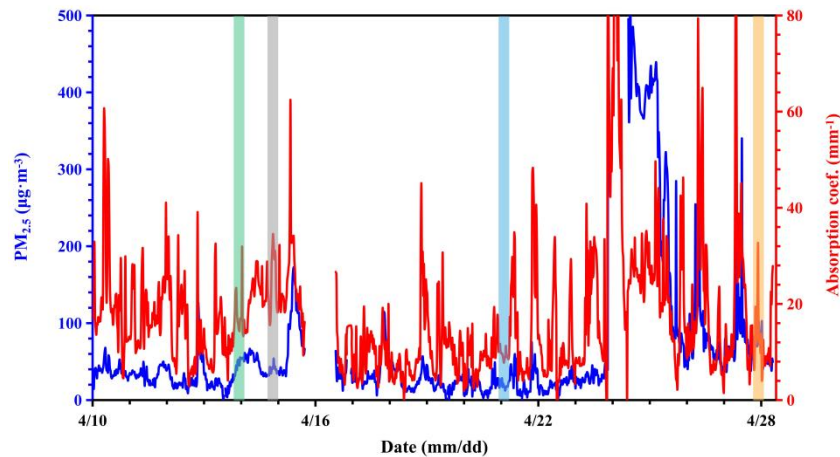


Fig. 2. Variations in $PM_{2.5}$ and absorption coefficient near the ground surface during April 2014 at Linze. The shadows in blue represent background aerosol, yellow dust, green polluted dust, and gray air pollutants.

low. In-situ measurements corroborate these low results for $PM_{2.5}$ and absorption coefficient (Fig. 2). However, the CR was large with a maximum value of 1.5, which may be due to the small backward signal of the background aerosols. Two of the wavelengths had the volume depolarization ratios < 0.2 , while the VDR_{532}/VDR_{355} ranged from 1.2 to 1.6 and VDR_{532} was larger than VDR_{355} from 200-700 m. Also, by integrating the spectra between 420 and 520 nm, we were able to characterize the wide fluorescence intensity (photon number). In Fig. 4(a), we can see that there is a small amount of anthropogenic pollutants around 300- 600 m, resulting in a certain fluorescence reaction, with a strength of less than 0.4.

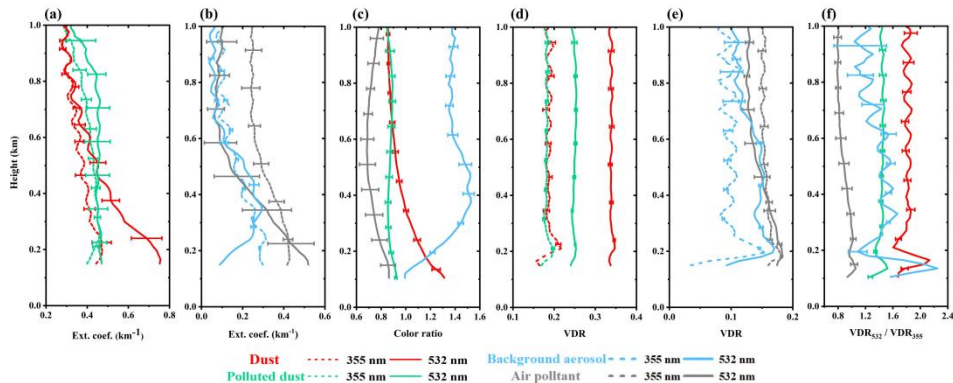


Fig. 3. Vertical profiles of extinction coefficients at 532 nm and 355 nm (a-b); color ratio (c); VDR at 532 nm and 355 nm (d-e) and VDR_{532}/VDR_{355} (f) from atmospheric aerosols observed by the lidar system for four aerosols.

2.2. Identification of the air pollutant particles

Figure 3 (b,c,e,f) depicts the vertical profiles of the particle characteristics during the air pollution aerosols incident on the evening of April 14, 2014. At night, researchers detected the typical air pollutant characteristic—a low depolarization, high extinction coefficient—in the 200-500 m

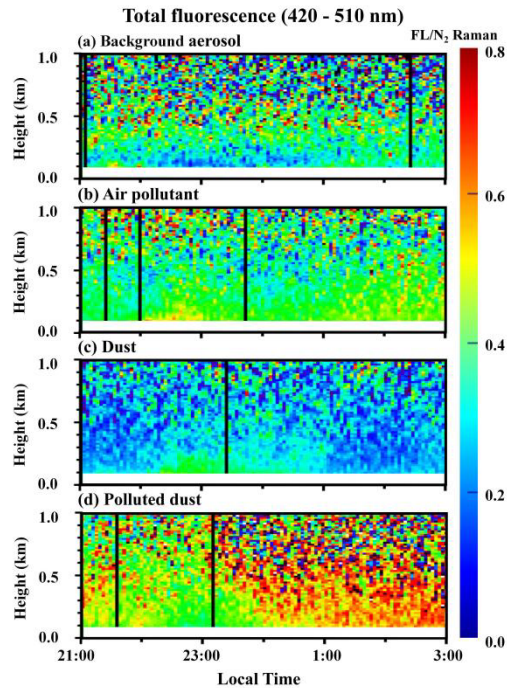


Fig. 4. Vertical structure of the total fluorescence signal between 420 and 510 nm for four aerosols: Background aerosols (a), Air pollutant (b), Dust (c) and Polluted dust (d).

height range. The particle depolarization ratio (PDR) of air pollutants at 355 nm was reported to be 0.09 ± 0.04 in South Africa by Giannakaki et al. [46], and 0.05 in Warsaw, Poland, by Janicka et al. [47]. The extinction coefficient at 532 nm was smaller than that at 355 nm and decreased very rapidly with height, from 0.4 km^{-1} to 0.1 km^{-1} . The CR was less than 0.8. The depolarization ratios of the two wavelengths are close, at about 0.16. Defined as the ratio of depolarization at 532 nm and 355 nm, Qi et al. [48] discovered that the $\text{VDR}_{532}/\text{VDR}_{355}$ can be utilized to assess dust and air pollution. $\text{VDR}_{532}/\text{VDR}_{355}$ of dust is greater than 1 while that of air pollutant is less than 1. In agreement with our findings, the $\text{VDR}_{532}/\text{VDR}_{355}$ for air pollutant is 0.98. Meanwhile, high fluorescence levels are another trait that will be used to differentiate air pollutants. Huffman et al. [49] also pointed out that pollutants have a high fluorescence ability, which provides theoretical support. Figure 4(b) illustrates the temporal development of the normalized fluorescence intensity for the air pollutant aerosols episode. Both of these variables changed during the course of the experiment. The overall fluorescence of polluted air was quite high, with readings as high as 0.5 for the course of the measurements.

2.3. Identification of the dust particles

A typical dust event measured is shown in vertical profiles of the particle parameters of EXT_{532} , EXT_{355} , CR, VDR_{532} , VDR_{355} and $\text{VDR}_{532}/\text{VDR}_{355}$ on 27-28 April in Fig. 3 (a,c,d,f). In the dust layer, the average EXT_{532} is larger than the EXT_{355} , but the average EXT_{532} decreased significantly with the increase in height from 0.7 km^{-1} to 0.4 km^{-1} . Lower aerosols have an average CR of around 1.2, falling to the upper aerosols' CR of about 0.9. However, there was hardly any variation in the VDR_{532} and VDR_{355} profiles between 200 and 600 meters, with values hovering around 0.34 and 0.19, respectively. And the high $\text{VDR}_{532}/\text{VDR}_{355}$, greater than 1.8, indicated that aerosol layer was particularly non-spherical. Figure 4(c) further shows that the

fluorescence signal was weak (0.26) between 1:00 and 3:00. As a result, the measured aerosol layer may as well be a pure dust layer.

2.4. Identification of the polluted dust particles

Aerosols are typically not of a single pure form, but rather a mixture of many types, which alters their optical and radiative properties. During transit, dust frequently combines with anthropogenic aerosols, producing polluted dust, which exacerbates environmental and climatic issues [50–52]. Figure 4(d) depicts a typical polluted dust layer below 1 km, complete with high fluorescence signals, confirming that dust can transport fluorescent aerosols. Figure 3 (a,c,d,f) depicts the equivalent vertical profiles of the particle properties of polluted dust. Huang et al. [53] report that the VDR can distinguish between clean dust and polluted dust. The average value of VDR for clean dust was higher than that for polluted dust, indicating that polluted dust was more spherical. The peak value of VDR for pure dust and polluted dust was 0.21 and 0.31, respectively. Freudenthaler et al. [21]. and Groß et al. [54]. both indicated that the particle depolarization ratio of pure dust aerosol was approximately 0.3 during Saharan Mineral Dust Experiment. These conclusions testify to our observations in Linze. It can be seen from Fig. 3 that VDR_{532} of polluted dust is around 0.25, while VDR_{532} of air pollutant aerosol is 0.17 and VDR_{532} of dust aerosol is 0.34. By contrast, the VDR_{355} is less different. Like the results of VDR_{532} , VDR_{532}/VDR_{355} have the largest value of dust, the second most polluted dust and the smallest air pollutant. So we believe that both VDR_{532} and VDR_{532}/VDR_{355} can be used as important characteristics to distinguish polluted dust and other aerosol types. When compared to the VDR profile, the EXT profile showed nearly constant change between 200 and 600 meters in both bands of polluted dust particles, with values hovering around 0.44. Consistent with Zhang et al. [55], we found that the CR for contaminated dust was close to 0.87, whereas for air pollutant aerosol it was larger than 0.76 and for dust aerosol it was less than 1.01. The CR of pure dust was often higher than that of polluted dust. Over a CR of 0.8, it was essentially pure dust. In the source regions, the CR values of dust particles were between 0.7 and 1.0 [56,57].

3. Discussion

When an ultraviolet laser interacts with an aerosol, a fluorescence spectrum is produced; the strength and peak wavelength of this spectrum depend on the substance being fluorescing [58,59]. Sugimoto et al. [60] showed that Asian dust and some of air-pollution aerosols transported from the urban and industrial areas are fluorescent. Aerosols can be characterized with the help of fluorescence measurements when they are taken in conjunction with other techniques, such as multi-wavelength Raman lidar or HSRL measurements of aerosol microphysical characteristics. Figure 5(a) displays the spectral data collected by the spectroscopic lidar system at the Linze site (39.05°N, 100.12°E, 1579 m) in April 2014. The data spans the wavelength range of 343 nm to 526 nm (channels 1 through 32). The signal intensity of the spectral channel at each height is normalized by the intensity of the nitrogen Raman scattering channel. The data demonstrates that gases in the atmosphere have robust Raman signals, particularly oxygen (376 nm), nitrogen (387 nm), and water vapor (407 nm). The spectra were broad, with no discernible features. Dust and polluted dust aerosols have slightly different spectral shapes, though. A peak at 461 nm was most prominent in the spectra of polluted dust, with a relatively narrow shoulder at 437 nm. Dust has a trough at 443 nm. Fluorescence intensity was greater in the air pollutant than in the background aerosols, and among the four spectra, polluted dust fluorescence was the strongest and dust fluorescence the weakest. The fluorescence intensity should depend on the aerosol density and the fluorescence efficiency. Aerosol fluorescence efficiency profiles are shown in Fig. 5(b) and the rough estimates of the standard deviations are shown as error bars. Even at night, the substantial inaccuracy from background radiation in the fluorescence measurement was a result of the wide spectral bandwidth. This was notably true between 700 and 1000

meters. Aerosols from air pollutants and polluted dust were found to be highly fluorescent [61,62]. The fluorescence efficiency of pure dust was less than 0.1. To a large extent, we attribute the fluorescence of polluted dust to bioaerosols bound to the dust's surface [63–65]. In order to further understand the contribution of fluorescence efficiency of different bands, the average fluorescence efficiency of 10 channels at 425–480 nm and the standard deviation are given, as shown in Fig. 6. We discovered that the efficiency of single-band fluorescence typically rises as the wavelength goes up. In addition, the relative size of fluorescence efficiency of the four aerosol particles are about polluted dust (4): air pollutant (8): background aerosols (2): dust (3).

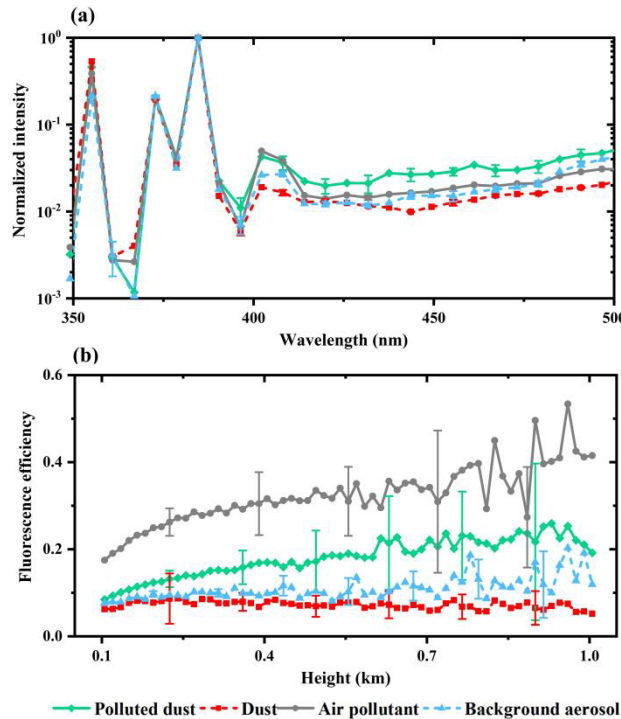


Fig. 5. (a) Normalised fluorescence spectra between 340–520 nm and vertical profiles of (b) fluorescence efficiency from atmospheric aerosols observed by the lidar system for four aerosols.

The campaign's aerosol parameters are summarized in Table 1. All nighttime observations have a 2-hour mean. We analyzed the correlation between the η , VDR, VDR_{532}/VDR_{355} and CR at wavelengths of 532 nm and 355 nm for common aerosols in Linze, such as air pollutants (A), dust (D), polluted dust (P), and background aerosols (B) to learn more about the discrepancies between the two wavelengths in aerosol observation data. Data sets of the four types were selected from lidar measurements in April. Figure 7(a)–(b) displays the connections between fluorescence efficiency and VDR for these four kinds at 532 nm and 355 nm. To classify aerosols, VDR_{532} was the most important metric since it showed the biggest variation between aerosol kinds. In contrast, a clear overlap existed between the numerical distributions of the VDR_{355} . The relationships between the fluorescence efficiency, CR and VDR_{532}/VDR_{355} for these four types are shown in Fig. 7(c)–(d). The distributions of VDR_{532}/VDR_{355} and CR for dust aerosols was wider than that for polluted dust. The correlation analysis revealed that the VDR_{532}/VDR_{355} was located within the ranges of 1.6–1.9 and 1.3–1.5 for pure dust aerosol and polluted dust aerosol and the fluorescence efficiency was located within the ranges of 0.04–0.12 and 0.08–0.16, respectively. However, the overlapping value for CR between 0.9 and 1.1 indicate that it is difficult

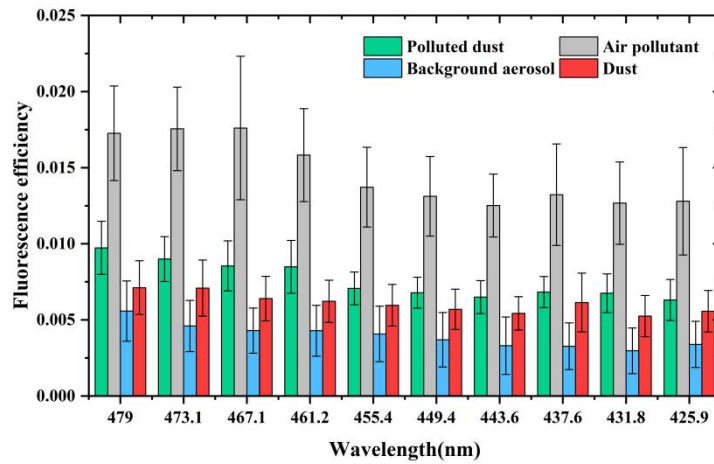


Fig. 6. Mean and standard deviation of fluorescence efficiency between 425.9 nm and 479 nm for four aerosols.

to distinguish four aerosols via the CR approach alone. Misclassification can be reduced with the use of additional parameters. The obtained results show that dust, polluted dust, and air pollutant may be distinguished using a combination of depolarization and fluorescence measurements.

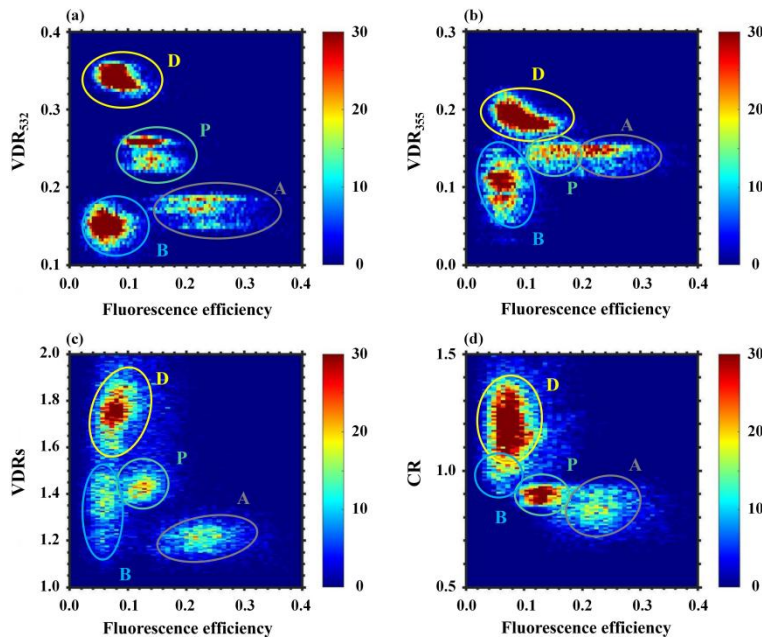


Fig. 7. Relationship between the fluorescence efficiency η and (a) VDR₅₃₂, (b) VDR₃₅₅, (c) VDR₅₃₂/VDR₃₅₅, (d) CR for air pollutants (A), dust (D), polluted dust (P) and background aerosol (B) over northwest China during April of 2014. The grid resolution is 500×500 .

Table 1. Summary of key optical properties of fluorescent aerosols observed by the developed lidar under different weather conditions over northwest China during April of 2014

Parameters	VDR ₅₃₂	VDR ₃₅₅	VDR ₅₃₂ / VDR ₃₅₅	EXT ₅₃₂ (km ⁻¹)	EXT ₅₃₂ (km ⁻¹)	CR	Total Fluor.	η
Background aerosols	0.15	0.10	1.52	0.25	0.23	1.44	0.32	0.10
Air pollutant	0.17	0.98	0.98	0.36	0.40	0.76	0.44	0.28
Dust	0.34	0.19	1.81	0.51	0.41	1.01	0.26	0.08
Polluted dust	0.25	0.18	1.43	0.45	0.44	0.87	0.66	0.17

4. Conclusion

We built a spectroscopic lidar system in this study to look into characterizing atmospheric bioaerosols close to dust sources in April 2014 in Linze. The constructed lidar system can not only allow us to measure the 32-channel fluorescent spectrum between 343 nm to 526 nm with an excitation wavelength of 355 nm but also simultaneously detect polarisation measurements at 355 nm and 532 nm, as well as Raman scattering signals at 387 nm and 407 nm. Using lidar data, we identified four regional aerosol particles and compared their physical and optical characteristics. It provides a new method for real-time study of range resolution fluorescence aerosol by lidar. According to the findings, the lidar system was able to pick up the robust fluorescence signal emitted by dust aerosols. It shows that the dust in Linze contains bioaerosols. The fluorescence efficiency may approach 0.17 for polluted dust in particular. Among the four fluorescence spectra, the fluorescence of polluted dust was the strongest and that of dust was the weakest. In the fluorescence bands, the fluorescence efficiency tends to increase with the increase of wavelength. To be used for quantitative fluorescent aerosol characterisation, however, more research is required. We plan to upgrade the technology in the future so that it has more detection bands and better separation accuracy. Using the lidar system will benefit studies in the fields of meteorology, biology, ecology, and medicine.

Funding. Fundamental Research Funds for the Central Universities (Izujbky-2022-kb10, Izujbky-2022-kb11); Higher Education Discipline Innovation Project– 111 Project (B 13045); Chinese Academy of Sciences (XK2022DXC005); The Collaborative Research Project of the National Natural Science Foundation of China (L2224041); Gansu Provincial Science and Technology Innovative Talent Program, the High-level Talent and Innovative Team Special Project (22JR9KA001); Self-supporting Program of Guangzhou Laboratory (SRPG22-007).

Disclosures. The authors declare no conflicts of interest.

Data availability. Data underlying the results presented in this paper are not publicly available at this time but may be obtained from the authors upon reasonable request.

References

1. K. Tang, Z. Huang, J. Huang, T. Maki, S. Zhang, and A. Shimizu, "Characterization of atmospheric bioaerosols along the transport pathway of Asian dust during the Dust-Bioaerosol 2016 Campaign," *Atmos. Chem. Phys.* **18**(10), 7131–7148 (2018).
2. C. E. Morris, D. C. Sands, M. Bardin, R. Jaenicke, B. Vogel, C. Leyronas, P. A. Ariya, and R. Psenner, "Microbiology and atmospheric processes: research challenges concerning the impact of airborne micro-organisms on the atmosphere and climate," *Biogeosciences* **8**(1), 17–25 (2011).
3. V. R. Després, J. Alex Huffman, Susannah M. Burrows, Hoose, Corinna, Aleksandr S. Safatov, and Aleksandr S. Buryak, "Primary biological aerosol particles in the atmosphere: a review," *Tellus Ser B Chem Phys Meteorol.* **64**(1), 15598 (2012).
4. P. Ginoux, J. M. Prospero, O. Torres, and M. Chin, "Long-term simulation of global dust distribution with the GOCART model: correlation with North Atlantic Oscillation," *Environ.model.software* **19**(2), 113–128 (2004).
5. H. Behzad, K. Mineta, and T. Gojobori, "Global Ramifications of Dust and Sandstorm Microbiota," *Genome Biol. Evol.* **10**(8), 1970–1987 (2018).
6. N. Yamaguchi, T. Ichijo, A. Sakotani, T. Baba, and M. J. R. Nasu, "Global dispersion of bacterial cells on Asian dust," *Scientific Reports* **2**(525) (2012).

7. S. Groß, V. Freudenthaler, K. Schepanski, C. Toledano, A. SchäFler, A. Ansmann, and B. Weinzierl, "Optical properties of long-range transported Saharan dust over Barbados as measured by dual-wavelength depolarization Raman lidar measurements," *Genome Biol. Evol.* **10**(8), 1970–1987 (2018).
8. K. Hara and D. Zhang, "Bacterial abundance and viability in long-range transported dust," *Atmos. Environ.* **47**, 20–25 (2012).
9. N. P. Hua, F. Kobayashi, Y. Iwasaka, G. Y. Shi, and T. Naganuma, "Detailed identification of desert-originated bacteria carried by Asian dust storms to Japan," *Aerobiologia* **23**(4), 291–298 (2007).
10. J. M. Prospero, E. Blades, G. Mathison, and R. Naidu, "Interhemispheric transport of viable fungi and bacteria from Africa to the Caribbean with soil dust," *Aerobiologia* **21**(1), 1–19 (2005).
11. T. Maki, R. Susuki, R. Kobayashi, R. Kakikawa, R. Tobo, R. Yamada, R. Higashi, R. Matsuki, R. Hong, and R. Hasegawa, "Phylogenetic analysis of atmospheric halotolerant bacterial communities at high altitude in an Asian dust (KOSA) arrival region, Suzu City," *Sci. Total Environ.* **408**(20), 4556–4562 (2010).
12. S. Ruske, D. O. Topping, V. E. Foot, A. P. Morse, and M. W. Gallagher, "Machine learning for improved data analysis of biological aerosol using the WIBS," *Atmos. Meas. Tech.* **11**(11), 6203–6230 (2018).
13. S. M. Daly, D. J. O'Connor, D. A. Healy, S. Hellebust, J. Arndt, E. J. McGillicuddy, P. Feeney, M. Quirke, J. C. Wenger, and J. R. Sodeau, "Investigation of coastal sea-fog formation using the WIBS (wideband integrated bioaerosol sensor) technique," *Atmos. Chem. Phys.* **19**(8), 5737–5751 (2019).
14. Y. L. Pan, "Detection and characterization of biological and other organic-carbon aerosol particles in atmosphere using fluorescence," *J. Quant. Spectrosc. Radiat. Transfer* **150**, 12–35 (2015).
15. A. Manninen, M. Putkiranta, J. Saarela, A. Rostedt, and T. Sorvajrvi, "Fluorescence cross sections of bioaerosols and suspended biological agents," *Appl. Opt.* **48**(22), 4320 (2009).
16. H. Enokido, C.W. Ugwu, K. Mitsumoto, K. Yabusaki, and H. Aoyagi, "Comparative analysis of autofluorescence and diameter for the spheroidal pollen of *Cryptomeria japonica* and *Chamaecyparis obtusa* pollen in Japan," *Jpn. J. Palynol* **54**, 69e77 (2008).
17. K. Mitsumoto, K. Yabusaki, K. Kobayashi, and H. Aoyagi, "Development of a novel real-time pollen-sorting counter using species-specific pollen autofluorescence," *Aerobiologia* **26**(2), 99–111 (2010).
18. F. Immler, D. Engelbart, and O. J. A. C. Schrems, "Fluorescence from atmospheric aerosol detected by a lidar indicates biogenic particles in the lowermost stratosphere," *Atmos. Chem. Phys.* **5**(2), 345–355 (2005).
19. V. Sivaprakasam, H. B. Lin, A. L. Huston, and J. D. Eversole, "Spectral characterization of biological aerosol particles using two-wavelength excited laser-induced fluorescence and elastic scattering measurements," *Opt. Express* **19**(7), 6191 (2011).
20. Y. Saito, K. Ichihara, K. Morishita, K. Uchiyama, F. Kobayashi, and T. Tomida, "Remote detection of the fluorescence spectrum of natural pollens floating in the atmosphere using a laser-induced-fluorescence spectrum (lifs) lidar," *Remote Sens.* **10**(10), 1533 (2018).
21. V. Freudenthaler, M. Esselborn, M. Wiegner, B. Heese, and M. Seefeldne, "Depolarization ratio profiling at several wavelengths in pure Saharan dust during SAMUM 2006," *Tellus B* **61**(1), 165–179 (2009).
22. Wei Wang, Wei Gong, and Feiyue Mao, "Physical Constraint Method to Determine Optimal Overlap Factor of Raman Lidar," *J. Opt* **47**(1), 83–90 (2018).
23. L. Mei, T. Ma, Z. Zhang, R. Fei, K. Liu, Z. Gong, and H. Li, "Experimental Calibration of the Overlap Factor for the Pulsed Atmospheric Lidar by Employing a Collocated Scheimpflug Lidar," *Remote Sensing* **12**(7), 1227 (2020).
24. J. Reichardt, O. Behrendt, and F. Laueremann, "Spectrometric fluorescence and Raman lidar: absolute calibration of aerosol fluorescence spectra and fluorescence correction of humidity measurements," *Atmos. Meas. Tech.* **16**(1), 1–13 (2023).
25. A. Ansmann, M. Riebesell, U. Wandinger, C. Weitkamp, and E. Voss, "Combined raman elastic-backscatter LIDAR for vertical profiling of moisture, aerosol extinction, backscatter, and LIDAR ratio," *Appl. Phys. B* **55**(1), 18–28 (1992).
26. S. Zhang, Z. Huang, M. Li, X. Shen, Y. Wang, Q. Dong, J. Bi, J. Zhang, W. Li, Z. Li, and X. Song, "Vertical Structure of Dust Aerosols Observed by a Ground-Based Raman Lidar with Polarization Capabilities in the Center of the Taklimakan Desert," *Remote Sensing* **14**(10), 2461 (2022).
27. F. G. Fernald, "Analysis of atmospheric lidar observations: Some comments," *Appl. Opt.* **23**(5), 652–653 (1984).
28. E. J. C. Welton and J. R. Campbell, "Micropulse lidar signals: Uncertainty analysis," *J. Atmos. Ocean. Technol* **19**, 2089–2094 (2002).
29. I. Veselovskii, Q. Hu, P. Goloub, T. Podvin, M. Korenskiy, O. Pujol, O. Dubovik, and A. Lopatin, "Combined use of Mie-Raman and fluorescence lidar observations for improving aerosol characterization: feasibility experiment," *Atmos. Meas. Tech.* **13**(12), 6691–6701 (2020).
30. Z. Liu, N. Nobuo, and T. Murayama, "Extinction-to-backscatter ratio of Asian dust observed with high-spectral-resolution lidar and Raman lidar," *Appl. Opt.* **41**(15), 2760 (2002).
31. N. Sugimoto and C. H. Lee, "Characteristics of dust aerosols inferred from lidar depolarization measurements at two wavelengths," *Appl. Opt.* **45**(28), 7468–7474 (2006).
32. A. HARRIG, B. Holger, J. Cristofer, V. Igor, E. Ronny, and A. Dietrich, "Depolarization and lidar ratios at 355, 532, and 1064 nm and microphysical properties of aged tropospheric and stratospheric Canadian wildfire smoke," *Atmos. Chem. Phys.* **18**(16), 11847–11861 (2018).

33. Q. Dong, Z. Huang, W. Li, Z. Li, X. Song, W. Liu, T. Wang, J. Bi, and J. Shi, "Polarization Lidar Measurements of Dust Optical Properties at the Junction of the Taklimakan Desert-Tibetan Plateau," *Remote Sens.* **14**(3), 558 (2022).
34. Z. Huang, S. Qi, T. Zhou, Q. Dong, X. Ma, S. Zhang, J. Bi, and J. Shi, "Investigation of aerosol absorption with dual-polarization lidar observations," *Opt. Express* **28**(5), 7028–7035 (2020).
35. Z. Huang, J. Huang, J. Bi, G. Wang, and W. Wang, "Dust aerosol vertical structure measurements using three MPL lidars during 2008 China-U.S. joint dust field experiment," *J. Geophys. Res.* **115**(D7), D00K15 (2010).
36. N. Sugimoto, Z. Huang, T. Nishizawa, I. Matsui, and B. Tatarov, "Fluorescence from atmospheric aerosols observed with a multi-channel lidar spectrometer," *Opt. Express* **20**(19), 20800–20807 (2012).
37. O. Dubovik, B. N. Holben, T. F. Eck, A. Smirnov, and I. Slutsker, "Variability of Absorption and Optical Properties of Key Aerosol Types Observed in Worldwide Locations," *J. Atmos. Sci.* **59**(3), 590–608 (2002).
38. A. Shimizu, N. Sugimoto, I. Matsui, K. Arao, I. Uno, T. Murayama, N. Kagawa, K. Aoki, A. Uchiyama, and A. Yamazaki, "Continuous observations of Asian dust and other aerosols by polarization lidars in China and Japan during ACE-Asia," *J. Geophys. Res.* **109**(D19), D19S17 (2004).
39. M. Tesche, A. Ansmann, D. Müller, D. Althausen, R. Engelmann, V. Freudenthaler, and S. Gro, "Vertically resolved separation of dust and smoke over Cape Verde using multiwavelength Raman and polarization lidars during Saharan Mineral Dust Experiment 2008," *J. Geophys. Res.* **114**(D13), D13202 (2009).
40. T. Nishizawa, N. Sugimoto, I. Matsui, A. Shimizu, Y. Hara, U. Itsushi, K. Yasunaga, R. Kudo, and S.-W. Kim, "Ground-based network observation using Mie-Raman lidars and multi-wavelength Raman lidars and algorithm to retrieve distributions of aerosol components," *J. Quant. Spectrosc. Radiat. Transfer* **188**, 79–93 (2017).
41. D. Müller, A. Ansmann, I. Mattis, M. Tesche, U. Wandinger, D. Althausen, and G. Pisani, "Aerosol-type-dependent lidar ratios observed with Raman lidar," *J. Geophys. Res.* **112**(D16), D16202 (2007).
42. B. D. Foy, S. P. Burton, R. A. Ferrare, C. A. Hostetler, J. W. Hair, C. Wiedinmyer, and L. T. Molina, "Aerosol plume transport and transformation in high spectral resolution lidar measurements and WRF-Flexpart simulations during the MILAGRO Field Campaign," *Atmospheric Chemistry Physics* **11**(7), (2010).
43. P. S. Burton, A. M. Vaughan, A. R. Ferrare, and A. C. Hostetler, "Separating mixtures of aerosol types in airborne High Spectral Resolution Lidar data," *Atmos. Meas. Tech.* **7**(2), 419–436 (2014).
44. M. Filonchyk, M. Peterson, and V. Hurynovich, "Air Pollution in the Gobi Desert Region: Analysis of Dust Storm Events," *Q J R Meteorol Soc* **147**, 1097–1111 (2021).
45. X. Wu, J. Liu, Y. Wu, X. Wang, X. Yu, J. Shi, J. Bi, Z. Huang, T. Zhou, and R. Zhang, "Aerosol optical absorption coefficients at a rural site in Northwest China: The great contribution of dust particles," *Atmos. Environ.* **189**, 145–152 (2018).
46. E. Giannakaki, P. G. V. Zyl, D. Müller, D. Balis, and M. Komppula, "Optical and microphysical characterization of aerosol layers over South Africa by means of multi-wavelength depolarization and Raman lidar measurements," *Atmos. Chem. Phys.* **16**(13), 8109–8123 (2016).
47. L. Janicka and I. S. Stachlewska, "Properties of biomass burning aerosol mixtures derived at fine temporal and spatial scales from Raman lidar measurements: Part I optical properties," *Atmospheric Chemistry Physics* **1–46** (2019).
48. S. Qi, Z. Huang, X. Ma, J. Huang, T. Zhou, S. Zhang, Q. Dong, J. Bi, and J. Shi, "Classification of atmospheric aerosols and clouds by use of dual-polarization lidar measurements," *Opt. Express* **29**(15), 23461–23476 (2021).
49. J. A. Huffman, A. E. Perring, N. J. Savage, B. Clot, B. Crouzy, F. Tummon, O. Shoshanim, B. Damit, J. Schneider, and V. Sivaprakasam, "Real-time sensing of bioaerosols: Review and current perspectives," *Aerosol Sci. Technol.* **54**(5), 465–495 (2020).
50. S. Shin, Y. Noh, K. Lee, and H. Lee, "Retrieval of the single scattering albedo of Asian dust mixed with pollutants using lidar observations," *Adv. Atmos. Sci.* **31**(6), 1417–1426 (2014).
51. M. Mehta, N. Singh, and Anshumali, "Global trends of columnar and vertically distributed properties of aerosols with emphasis on dust, polluted dust and smoke - inferences from 10-year long CALIOP observations," *Remote Sensing of Environment* **208**, 120–132 (2018).
52. Z. Wang, C. Liu, Q. Hu, Y. Dong, H. Liu, C. Xing, and W. Tan, "Quantify the Contribution of Dust and Anthropogenic Sources to Aerosols in North China by Lidar and Validated with CALIPSO," *Remote Sens.* **13**(9), 1811 (2021).
53. J. P. Huang, J. J. Liu, B. Chen, and S. L. Nasiri, "Detection of anthropogenic dust using CALIPSO lidar measurements," *Atmos. Chem. Phys.* **15**(20), 11653–11665 (2015).
54. S. Groß, M. Tesche, V. Freudenthaler, C. Toledano, and M. Wiegner, "Characterization of Saharan dust, marine aerosols and mixtures of biomass-burning aerosols and dust by means of multi-wavelength depolarization and Raman lidar measurements during SAMUM 2," *Tellus B* **63**(4), 706–724 (2011).
55. Z. Zhang, J. Huang, B. Chen, Y. Yi, J. Liu, J. Bi, T. Zhou, Z. Huang, and S. Chen, "Three-Year Continuous Observation of Pure and Polluted Dust Aerosols Over Northwest China Using the Ground-Based Lidar and Sun Photometer Data," *J. Geophys. Res. Atmos.* **124**(2), 1118–1131 (2019).
56. J. Huang, J. Ge, and F. Weng, "Detection of Asia dust storms using multi-sensor satellite measurements," *Remote Sensing of Environment* **110**(2), 186–191 (2007).
57. Y. He and F. Yi, "Dust aerosols detected using a ground-based polarization lidar and CALIPSO over Wuhan (30.5 N, 114.4 E), China," *Advances in Meteorology*, **2015**, 1–18 (2015).
58. M. A. Stowers, A. Wuijckhuijse, J. Marijnnissen, C. E. Kientz, and T. Ciach, "Fluorescence preselection of bioaerosol for single-particle mass spectrometry," *Appl. Opt.* **45**(33), 8531–8536 (2006).

59. I. Veselovskii, N. Kasianik, M. Korenskii, Q. Hu, P. Goloub, T. Podvin, and D. Liu. “Multiwavelength fluorescence lidar observations of fresh smoke plumes”. (2023).
60. N. Sugimoto, Z. Huang, T. Nishizawa, I. Matsui, B. Tatarov, N. Sugimoto, U. N. Singh, A. Jayaraman, J. Huang, and D. Mueller, “Study of fluorescence of atmospheric aerosols using a lidar spectrometer,” In: *Lidar Remote Sensing for Environmental Monitoring XIII*. 8526(2013).
61. B. Li, S. Chen, Y. Zhang, H. Chen, and P. Guo, “Fluorescent aerosol observation in the lower atmosphere with an integrated fluorescence-Mie lidar,” *J. Quant. Spectrosc. Radiat. Transfer* **227**, 211–218 (2019).
62. I. Veselovskii, Q. Hu, P. Goloub, T. Podvin, B. Barchunov, and M. Korenskii, “Combining Mie–Raman and fluorescence observations: a step forward in aerosol classification with lidar technology,” *Atmos. Meas. Tech.* **15**(16), 4881–4900 (2022).
63. A. Hervàs, L. Camarero, I. Reche, and E. O. Casamayor, “Viability and potential for immigration of airborne bacteria from Africa that reach high mountain lakes in Europe,” *Environ. Microbiol.* **11**(6), 1612–1623 (2009).
64. T. Maki, Y. Kurosaki, K. Onishi, K. C. Lee, S. B. Pointing, D. Jugder, N. Yamanaka, H. Hasegawa, and M. Shinoda, “Variations in the structure of airborne bacterial communities in Tsogt-Ovoo of Gobi desert area during dust events,” *Air Quality Atmosphere Health* **10**(3), 249–260 (2017).
65. E. Federici, C. Petroselli, E. Montalbani, C. Casagrande, and D. Cappelletti, “Airborne bacteria and persistent organic pollutants associated with an intense Saharan dust event in the Central Mediterranean,” *Sci. Total Environ.* **645**, 401–410 (2018).